

ORIGINAL ARTICLE

Open Access



Effect of Cycling Low Velocity Impact on Mechanical and Wear Properties of CFRP Laminate Composites

Yang Sun¹, Zhen-Bing Cai^{1*}, Song-Bo Wu¹, Jian-Hua Liu¹ and Jia-Xin Yu²

Abstract

The mechanical and wear properties of CFRP laminate were investigated using a method of cycling low velocity impact, to study the trend and mechanism of impact resistance of the CFRP laminate under repeated impact during its service process. The interface responses of CFRP laminate under different impact kinetic energy during the cycling impact process were studied experimentally, such as impact contact duration, deformation and energy absorption. The worn surface morphologies were observed through optical microscopy and a 3-D surface profiler and the cross-sectional morphologies were observed through SEM to investigate the mechanism of impact material damage. Based on a single-degree-of-freedom damping vibration model, the normal contact stiffness and contact damping of the material in different wear stages were calculated. It shows the failure process of CFRP laminate damaged by accumulated absorption energy under the cycling impact of different initial kinetic energy. The results indicate that the stiffness and damping coefficients will change at different impact velocities or cycle numbers. The damage mechanism of CFRP laminates under cycling low kinetic energy is delamination. After repeated experiments, it was found that there was a threshold value for the accumulated absorption energy before the failure of the CFRP laminate.

Keywords: CFRP laminate, Low velocity impact, Impact resistance, Accumulated absorption energy threshold, Delamination

1 Introduction

Carbon fiber reinforced plastic (CFRP) is a well-known composite with high tensile strength and low density and is used to manufacture satellites [1], airplanes [2], sports cars [3], and wind power generation equipment [4]. However, CFRP materials also have many drawbacks. For example, CFRP materials exhibits low tolerance against damage, such as delamination due to impact damage. CFRP materials internally delaminate when subjected to a cycling low-velocity impact load because of their low energy absorption capability; this weakness is one of the major failures of the CFRP material [5, 6]. Because of the common erosion of gravel [7] and the periodically mechanical vibration [8] during the work process, the

components made by CFRP laminate encounter cycling impact, which may lead to CFRP laminate delamination and equipment failure.

The investigation of the failure of CFRP laminate is mainly focused on the different ranges of impact velocity [9, 10], material properties [11], loading conditions [12–14], surface treatment methods [15], and failure prediction using FEM [16, 17]. Various studies have investigated the impact damage and response of CFRP laminate. He et al. [18–20], Petronyuk et al. [21] and Boccardi et al. [22] have done considerable research on the nondestructive testing methods of composite laminate subjected to impact loads through the techniques of pulsed eddy current (PEC), impulse acoustic microscopy and infrared thermography. Jang et al. [23–26] has investigated the impact signals obtained from the high-speed fiber Bragg grating (FBG) sensor system on CFRP laminates. Through this method of analyzing the FBG sensor signal, locating the impact source and detecting delamination

*Correspondence: czb-jiaoda@126.com

¹ Tribology Research Institute, Key Lab of Advanced Technologies of Materials, Southwest Jiaotong University, Chengdu 610031, China
Full list of author information is available at the end of the article

damage of the material in real time is possible. Palazzetti et al. [27–30] has done a lot of research about the effect of nanofibrous on mechanical properties of polymeric composite materials. Saito et al. [31] has studied the effect of ply thickness on impact damage to CFRP laminates. Aoki et al. [32] has investigated the effect of hydrothermal conditions on CFRP laminates' impact strength.

The test method for the impact resistance of composite materials and metal materials is mainly Charpy impact test method [33–35]. The drawbacks of this single-impact test method are lacking of interface response data during the impact contact process, and cannot detect the effect of accumulated absorption energy on material properties. Cai et al. [36–38] have proposed studying the constant kinetic energy impact of the experimental method with high sampling ratio. It makes it possible to measure the effect of interface response and cumulative absorption energy on material properties during impact contact process. This research is based on an independently developed low-velocity equipment for impact experiments with the constant kinetic energy impact of the experimental method. In this study, we investigate the dynamic response, energy absorption, and mechanical response formula of CFRP laminate plates. In addition, the relationships among the stiffness and damping coefficients versus impact velocity and impact cycles have been explored.

2 Materials and Methods

2.1 Experiment Methods

A low-velocity impact wear experiment apparatus (Figure 1) was used to simulate the impact process in different modes. In this experiment, the impact power source is a voice coil motor (9), which pushes the impact block (7) to produce the initial kinetic energy. The impact block slides on the rail (6) and hits the specimens (3) with the impact head (4). The rebound energy in the impact block is then absorbed by the damping punch (8).

This test device has two sensors, namely, a motion detector (5), which records position as a function of time during the impact process, and a force sensor (1) behind the support structure (2) of specimens that records the inertial force of the impact block when the impact head hits the specimens. All the data will be received by a controller and sent to a software on a PC.

2.2 Experiment Materials

In these experiments, the specimens are carbon fiber reinforced epoxy laminates with a diameter of 25 mm and thickness of 1 mm. The impact heads are made of 304 stainless steel ball head cylinders and have a diameter of 2 mm. The total mass of the impact block, impact head, and rail is approximately 570 g. The experiments

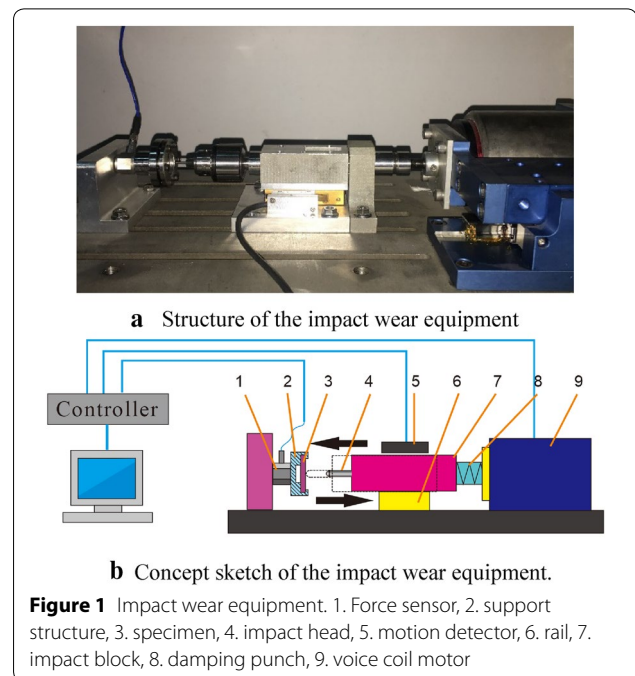


Figure 1 Impact wear equipment. 1. Force sensor, 2. support structure, 3. specimen, 4. impact head, 5. motion detector, 6. rail, 7. impact block, 8. damping punch, 9. voice coil motor

are tested by the different parameters of the initial impact velocity (Table 1).

The CFRP laminate specimens are composed of multi-layered carbon fiber bonded by epoxy. The top and bottom layers of the carbon fiber are orthogonally woven (TORAYCA[®] cloth) and the intermediate carbon fiber layers are unidirectional (TORAYCA[®] prepreg) and alternately arranged (Figure 2(a)). All carbon fibers used in CFRP laminate specimens are TORAYCA[®] yarn (T700SC-12000) with a tensile strength of 4900 MPa and a tensile modulus of 230 GPa.

In our experiment, the CFRP laminate specimens are fixed by a support structure (Figure 1(b)) as a ring area. The diameter of the flexible area is 20 mm (Figure 2(b)).

2.3 Analysis and Testing

After the test, the surface morphology of the sample was observed under an optical microscope (OM, OLYMPUS-BX60M) and a 3-D surface profiler. The cross-sectional morphology was analyzed by the SEM. Data were recorded using a motion detector and a force sensor throughout the experiment to investigate the response and damage mechanism.

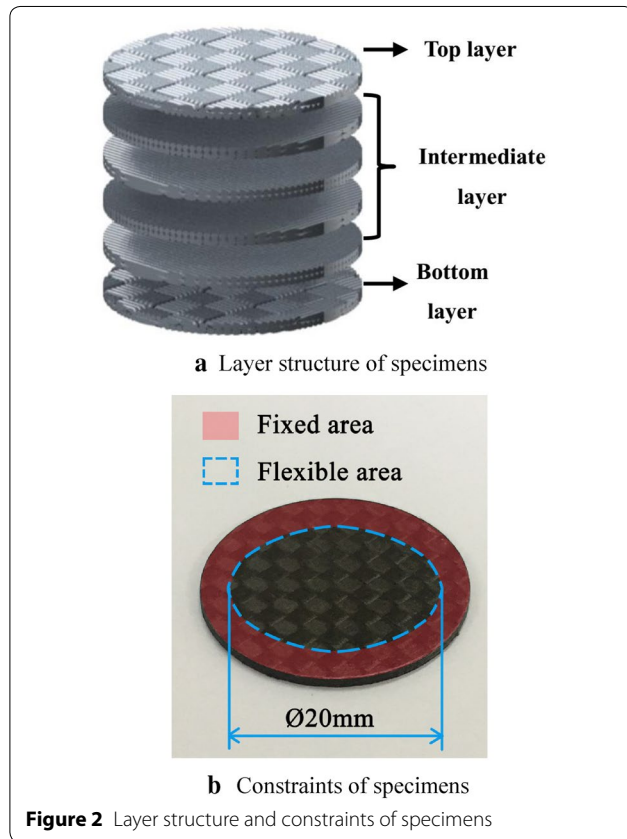
3 Results and Discussion

3.1 Interface Responds

During the experiment, the data on contact force signal and motion signal were collected at multiple sampling points.

Table 1 Test parameter

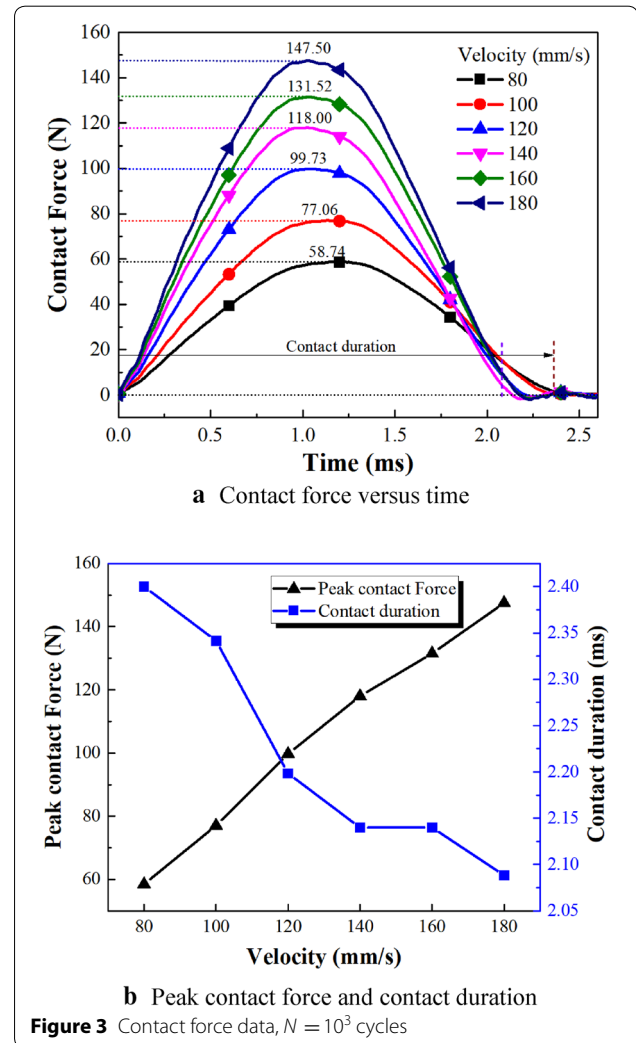
Test no.	1#	2#	3#	4#	5#	6#
Velocity (mm/s)	80	100	120	140	160	180



The impact force data at the impact cycle of 1000 is shown in Figure 3. When the initial impact velocity increases, the peak value of the impact force increases proportionally and the contact duration decreases slightly. The contact duration is approximately 2.30 ms and the peak contact force is 58.74 N when the initial impact velocity is 80 mm/s. The peak contact force increases to 147.50 N and the contact duration decreases to 2.08 ms when the initial impact velocity is 180 mm/s.

Changes in contact duration and peak contact force throughout the experiment are illustrated in Figure 4(a) and (b). Peak contact force slightly increases and contact duration slowly decreases when the initial impact velocity is not higher than 120 mm/s.

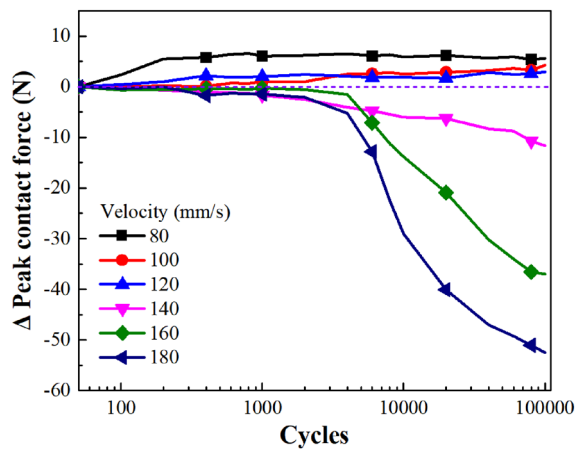
When the initial impact velocity is higher than 120 mm/s, the contact duration increases and the peak contact force decreases with an increase in the impact cycle. When the initial impact velocity is not lower than



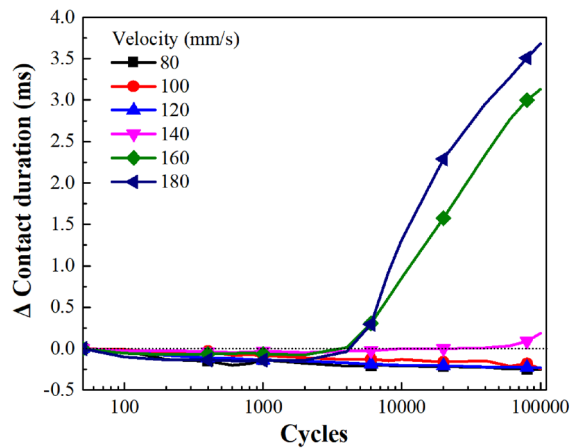
160 mm/s, the impact of the contact force sharply drops and the contact duration quickly rises after a number of impact cycles.

The motion data of the impact block during the impact process stands for the deflection of the CFRP specimen, the 1000th cycle's impact of which is shown in Figure 5(a). The maximum deflection of the specimen increases with the initial impact velocity.

Separating the motion data of the impact block, we obtain the velocity of the impact block, the 1000th cycle's impact of which is shown in Figure 5(b). The error of the initial impact velocity is less than 2%. The higher the



a Change of peak contact force



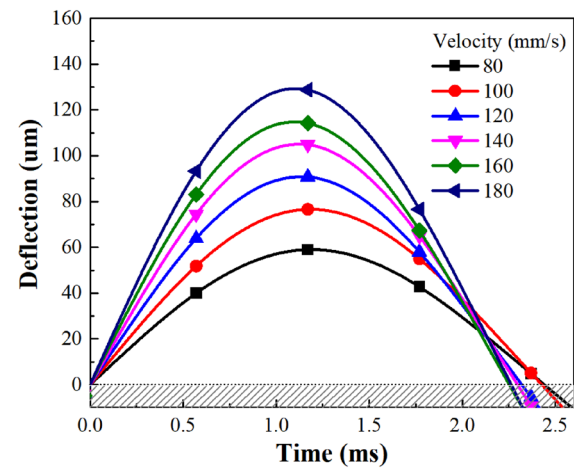
b Change of contact duration

Figure 4 Change of peak force and contact duration throughout impact process

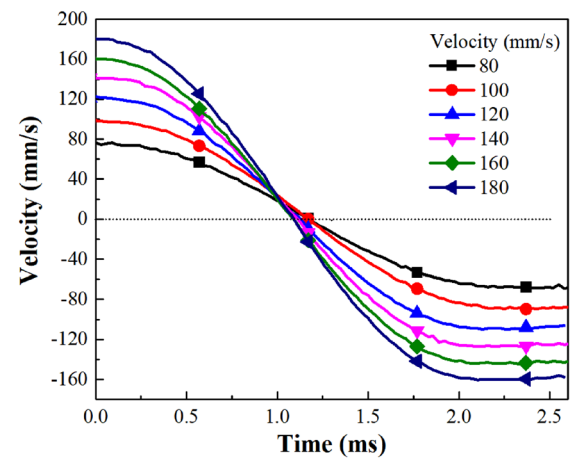
initial impact velocity, the lower the time cost of reducing the impact block velocity to zero.

By calculating the velocity of the impact block, we obtain the latter's kinetic energy during the impact process, the 1000th cycle's impact of which is shown in Figure 5(c). The ratio of kinetic energy absorption is stabilized at approximately 25% at the 1000th impact cycle.

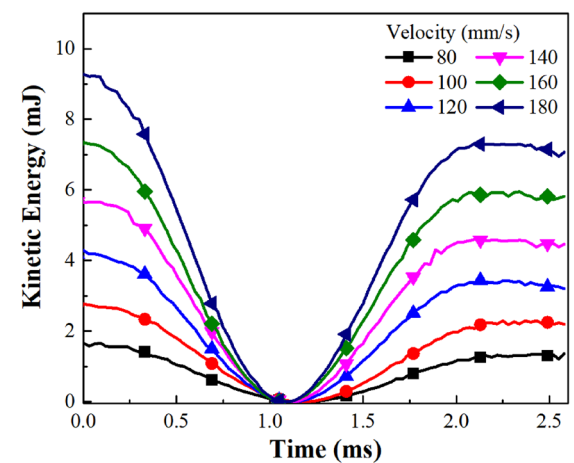
Changes in the absorbed kinetic energy throughout the experiment are shown in Figure 6. The absorbed energy does not significantly change when the initial impact velocity is not higher than 100 mm/s and slowly decreases when the initial impact velocity is not higher than 140 mm/s. When the initial impact velocity is not lower than 160 mm/s, the absorbed kinetic energy increases rapidly at approximately the 4000th impact cycle and falls after the 10000th impact cycle.



a Deflection of specimen tubes



b Velocity of impact block



c Kinetic energy

Figure 5 Motion data of impact block, $N = 10^3$ cycles

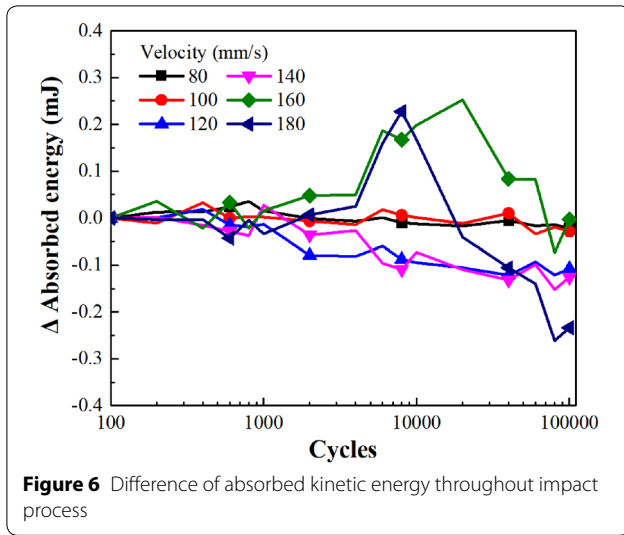


Figure 6 Difference of absorbed kinetic energy throughout impact process

3.2 Wear Behavior

Figure 7 shows surface morphology under an OM. Figure 8 and Figure 9 show the 3-D profile and cross-sectional morphology of the wear scar after 10^5 cycles of impact. The area, depth, and volume of the wear scar grow with an increasing initial impact velocity. When the initial impact velocity is 160 mm/s or higher, noticeable cracks surround the wear scar. When the initial impact velocity is higher than 180 mm/s, big radial cracks appear on the surface of the wear scars.

The area and volume of wear scars and cumulative absorbed energy are shown in Figure 10. Observing the volume and area of wear scars, a high correlation ($\rho = 0.9899$) between energy absorption and wear area emerges. However, the volume of wear scars at the initial impact velocities of 160 mm/s and 180 mm/s increases more than that at a lower initial impact velocity. In addition, energy absorption and wear volume exhibit a lower correlation ($\rho = 0.9352$). The correlation coefficient is calculated by Eq. (1):

$$\rho_{X,Y} = \text{corr}(X,Y) = \frac{\text{cov}(X,Y)}{\sigma_X \sigma_Y}. \quad (1)$$

Figure 11 shows the cross-sectional topography of the wear scars under SEM at the magnification of 200 after 10^5 cycles of impact. As shown in Figure 11(a), the specimens are barely worn, and no cracks appear at the impact velocity of 120 mm/s. When the impact velocity approaches 140 mm/s, broken carbon fibers appear in the wear scar, and delamination cracks appear behind the first layer (Figure 11(b)). In Figure 11(c), we find that delamination appears in top layer under the impact area.

Furthermore, big cracks appear behind the first layer while many small cracks emerge between the rest layers (Figure 11(d)).

3.3 Stiffness and Damping Characteristic Analysis

As shown in Figure 12(a), the power curve of the impact force can be obtained by multiplying the velocity of the impact block (Figure 5(b)) with the contact force (Figure 3). Integrating the power curve of the impact force produces the work data of the impact force (Figure 12(b)).

Comparing the kinetic energy of the impact block (Figure 5(c)) with the work data of the impact force (Figure 12(b)), the difference between the work done by the impact force and the absorbed kinetic energy appears to be considerably small, leading us to believe that the external disturbance will not affect the impact process. The residual kinetic energy in the sample is significantly small when the impact head and the sample separation are separated because the mass of the sample (approximately 0.7 g) is considerably smaller than that of the impact block (570 g).

The impact process can be simplified as a single-degree-of-freedom (SDoF) vibration model (Figure 13) when disregarding external disturbance forces and the effect of the specimens' mass. We divide the impact contact force (F_{impact}) into two separate parts, namely, the elastic force part (F_K) and the damping force part (F_C), as shown in Eqs. (2)–(4). The elastic force is generated by the conversion process of the impact block's kinetic energy and the elastic potential of the specimen and has a direction opposite to where the specimens are deflected. The damping force occurs during plastic deformation, delamination, fracture, and impact friction and has a direction opposite to that of the impact block's velocity.

$$F_{\text{impact}} = F_K + F_C, \quad (2)$$

$$F_K = K \cdot X, \quad (3)$$

$$F_C = C \cdot \dot{X}. \quad (4)$$

We speculate that the generalized stiffness coefficient (K) and the generalized damping coefficient (C) can be expressed by Eqs. (5) and (6):

$$K = k \cdot X^p, \quad (5)$$

$$C = c \cdot X^m \cdot \dot{X}^n. \quad (6)$$

Importing the impact contact force data and deformation data into Eqs. (5) and (6) obtains the fitting results in Eqs. (7) and (8). The comparison of fitted contact force and actual contact force data at a velocity of 180 mm/s after 1000 impact cycles is shown in Figure 14. The curves of the elastic force (F_K) and the damping force (F_C)

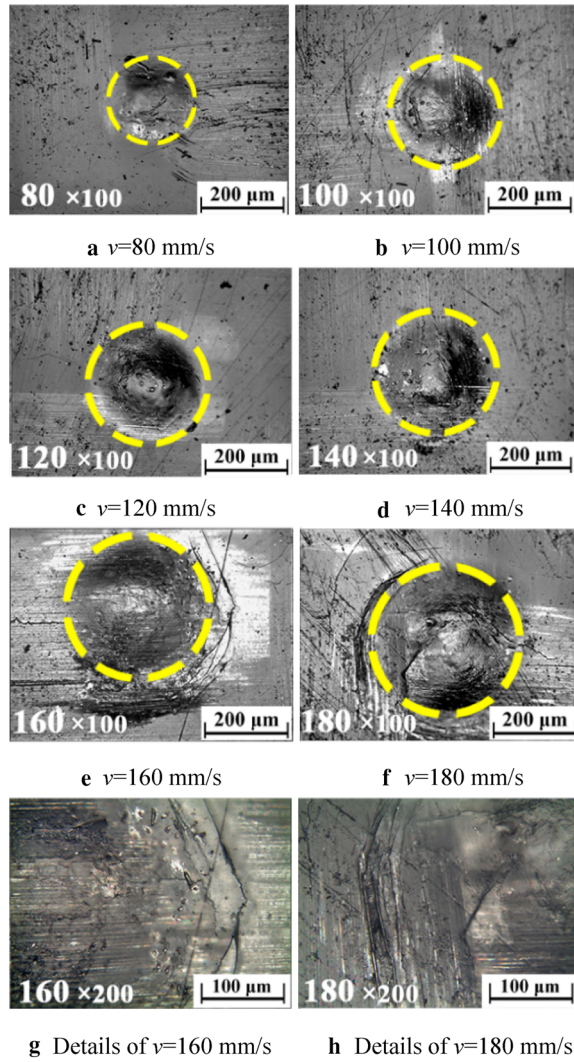


Figure 7 Surface morphology of wear scars under optical microscope, $N = 10^5$ cycles

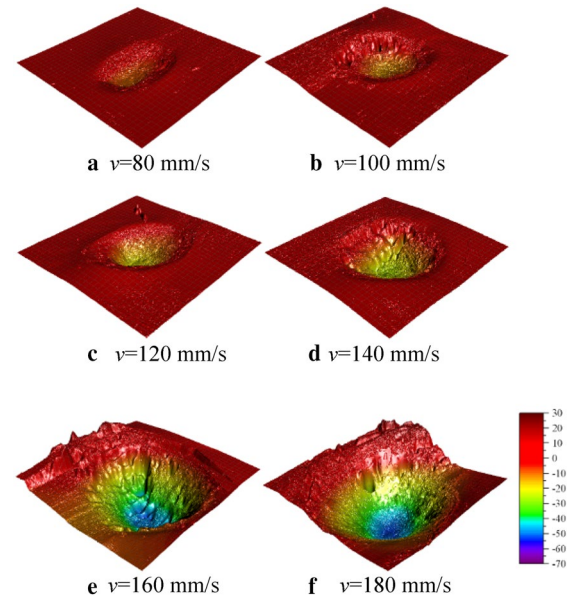


Figure 8 3-D Profile of wear scars, $N = 10^5$ cycles

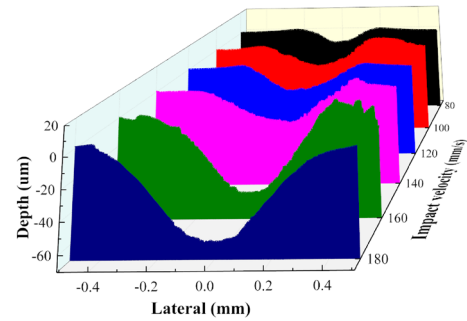


Figure 9 Cross-sectional morphology of wear scars, $N = 10^5$ cycles

at the 1000th impact is shown in Figure 15(a) and (b). In all curves of the fitted contact force, r^2 is not less than 0.9999.

$$F_K = k \cdot X^{1.36}, \quad (7)$$

$$F_C = c \cdot X^{0.75} \cdot \dot{X}^2. \quad (8)$$

Substituting the contact force data and deflection data into Formulas 7 and 8 obtains the stiffness coefficient (K) and the damping coefficient (C) throughout the experiment. The linear fitting of the stiffness coefficient and damping coefficient data are shown in Figure 16.

In Figure 16(a), the stiffness coefficient is lower when the initial impact velocity is higher. When the initial impact velocity is lower than 120 mm/s, the stiffness

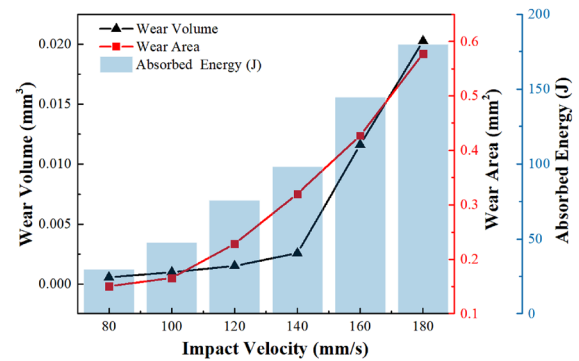


Figure 10 Area, volume of wear scars and cumulative absorbed energy, $N = 10^5$ cycles

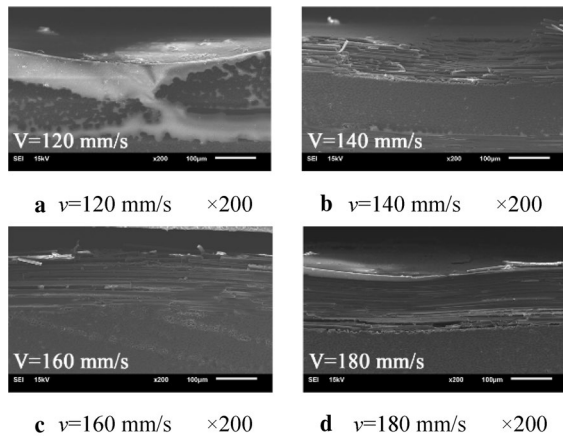
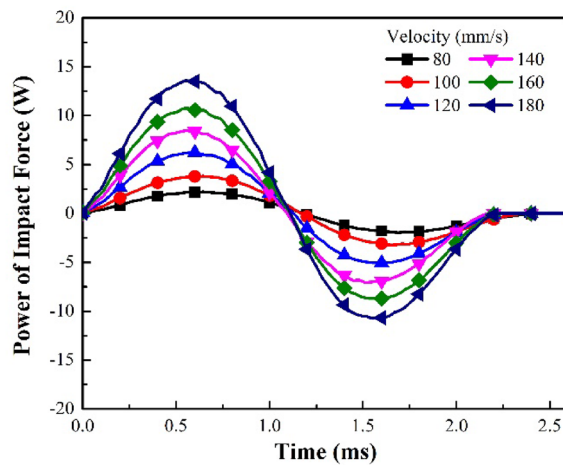
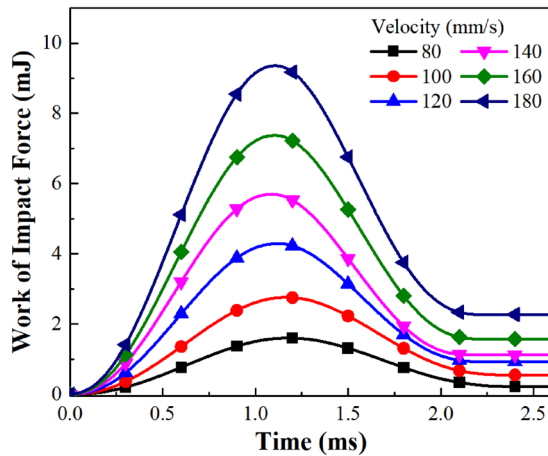


Figure 11 Cross-sectional topography of wear scars under SEM, $N = 10^5$ cycles



a Power of contact force



b Work of contact force

Figure 12 Power and work of contact force, $N = 10^3$ cycles

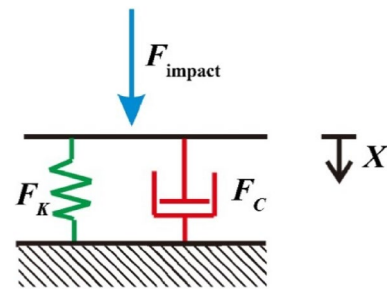


Figure 13 SDOF damped vibration model

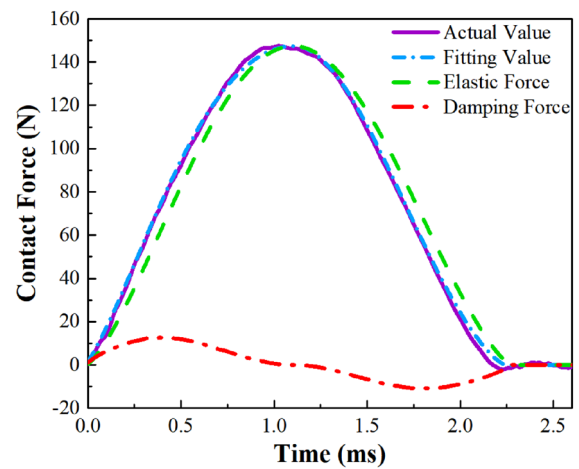
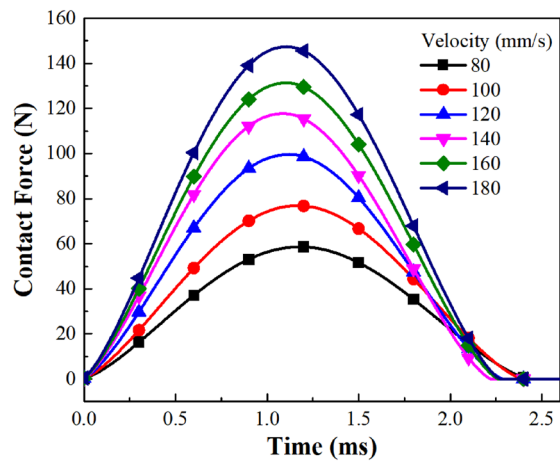


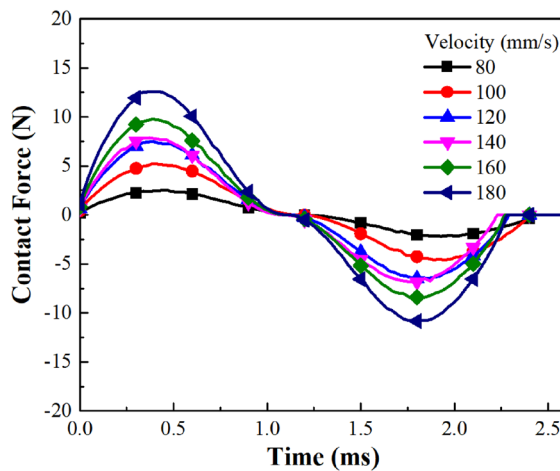
Figure 14 Fitted contact force and actual contact force data, $v = 180$ mm/s, $N = 10^3$ cycles

coefficient decreases as the number of impact cycles increases. However, when the initial impact velocity is higher than 140 mm/s, the stiffness coefficient increases as the number of impact cycles increases. The stiffness coefficient decreases rapidly after approximately 6000–8000 times of impact when the initial impact velocity is higher than 160 mm/s.

Figure 16(b) shows that the damping coefficient does not significantly change at different initial impact velocities. When the initial impact velocity is lower than 120 mm/s, the damping coefficient slowly increases as the number of impact cycles increases. However, when the initial impact velocity is higher than 140 mm/s, the damping coefficient decreases slowly as the number of impact cycles increases. The damping coefficient decreases rapidly after approximately 6000–8000 times of impact when the initial impact velocity is higher than 160 mm/s.



a Elastic force



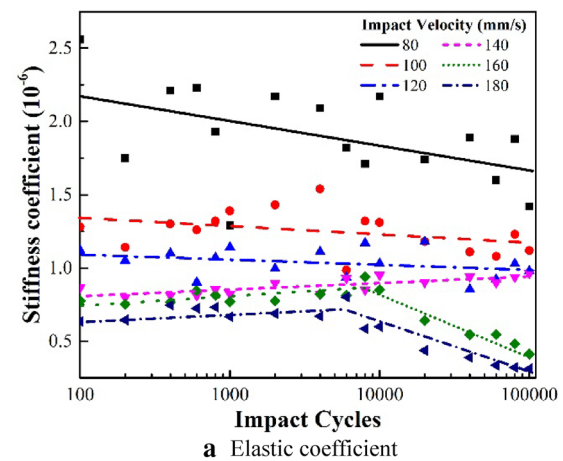
b Damping force

Figure 15 Elastic force and damping force, $N = 10^3$ cycles

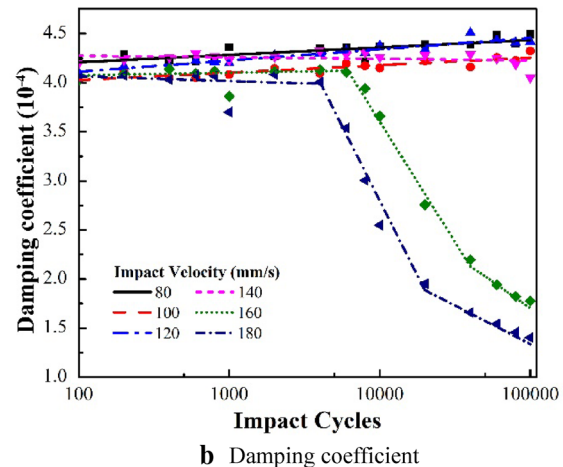
4 Conclusions

In this research, the impact wear and interface response behavior of a CFRP laminate under different initial impact energy levels were investigated. It presents a method of testing CFRP laminates' response under continuous impact. The way to predict CFRP materials' failure based on dynamic response and energy absorption thresholds is subject to further study. Several conclusions were drawn from the results.

- (1) When the impact energy is changed by changing the initial impact velocity, the peak value of the impact contact force increases linearly with the impact velocity and the contact time decreases slightly with the increase in impact velocity.
- (2) Energy absorption and wear area are highly correlated ($\rho = 0.9899$). However, the volume of the wear



a Elastic coefficient



b Damping coefficient

Figure 16 Stiffness coefficient and damping coefficient, $N = 10^3$ cycles

scars at the initial impact velocities of 160 mm/s and 180 mm/s increases more than that at lower initial impact velocities due to the delamination of the specimens. Also, it results in a lower correlation ($\rho = 0.9352$) between energy absorption and wear volume.

- (3) The stiffness coefficient and the damping coefficient of the CFRP laminate specimens are calculated by fitting Eqs. (7) and (8). The stiffness coefficient is lower when the impact velocity is higher. However, the change in the damping coefficient at different impact velocities is not considerable. When the CFRP laminate specimens delaminate, the stiffness coefficient and the damping coefficient decrease rapidly with an increase in the number of experiment cycles.
- (4) The delamination of the CFRP laminate specimens occurs only in experiments with high initial impact

velocities (160 mm/s and 180 mm/s). The specimens delaminate after 6000–8000 times of impact rather than in the beginning of the experiment. The correlation between delamination and cumulative energy absorption is low. Therefore, we assume that a threshold for absorbed energy exists during a single impact to the CFRP laminate specimens to be delaminated.

Authors' Contributions

Z-BC was in charge of the whole trial; YS wrote the manuscript; S-BW assisted with sampling and laboratory analyses; J-XY provided necessary help during the process of analyses. All authors read and approved the final manuscript.

Author Details

¹ Tribology Research Institute, Key Lab of Advanced Technologies of Materials, Southwest Jiaotong University, Chengdu 610031, China. ² Key Laboratory of Testing Technology for Manufacturing Process of Ministry of Education, Southwest University of Science and Technology, Mianyang 621010, China.

Authors' Information

Yang Sun, born in 1991, is currently a master candidate at *Institute of tribology, Southwest Jiaotong University, China*. He received his bachelor degree from *Beijing Institute of Technology, China*, in 2013. His research interests include impact fretting wear and development of equipment.

Zhen-Bing Cai, born in 1981. He received his PhD degree in materials science from *Southwest Jiaotong University, China*, in 2009. He joined the *School of Mechanical Engineering, Southwest Jiaotong University, China* from 2009. His current position is a professor and the deputy director of the Tribology Research Institute. His research areas cover the tribology of electrical contact system, aviation and nuclear power equipment.

Song-Bo Wu, born in 1992, is currently a master candidate at *Institute of tribology, South West Jiaotong University, China*. He received his bachelor degree from *Henan Polytechnic University, China*, in 2016.

Jian-Hua Liu, born in 1992, is currently a postdoctor in *South West Jiaotong University, China*. He received his PhDs degree from *South West Jiaotong University, China*, in 2016.

Jia-Xin Yu, born in 1982, is currently a professor at *Institute of Manufacturing Science and Engineering, South West University of Science and Technology, China*. He received his PhD degree on mechanical design and theory from *South West Jiaotong University, China*, in 2011.

Acknowledgements

The authors sincerely thank Professor Min-Hao Zhu of *Southwest Jiaotong University* for his critical discussion and reading during manuscript preparation.

Competing Interests

The authors declare that they have no competing interests.

Funding

Supported by National Natural Science Foundation of China (Grant Nos. U1530136, 51627806), Young Scientific Innovation Team of Science and Technology of Sichuan Province of China (Grant No. 2017TD0017), and Opening Project of Key Laboratory of Testing Technology for Manufacturing Process of China (Grant Nos. 2016-01, Southwest University of Science and Technology).

Publisher's Note

Springer Nature remains neutral with regard to jurisdictional claims in published maps and institutional affiliations.

Received: 3 February 2018 Accepted: 21 November 2018
Published online: 27 December 2018

References

- [1] F Schäfer, R Destefanis, S Ryan, et al. Hypervelocity impact testing of CFRP/Al honeycomb satellite structures. In: *4th European Conference on Space Debris*, 2005, 587: 407.
- [2] Y Miyano, M Nakada, K Nishigaki. Prediction of long-term fatigue life of quasi-isotropic CFRP laminates for aircraft use. *Int. J. Fatigue*, 2006, 28(10): 1217-1225.
- [3] J R Duflou, J De Moor, I Verpoest, et al. Environmental impact analysis of composite use in car manufacturing. *CIRP Ann. Manuf. Techn.*, 2009; 58(1): 9-12.
- [4] W X Wang, T Matsubara, J Hu, et al. Experimental investigation into the influence of the flanged diffuser on the dynamic behavior of CFRP blade of a shrouded wind turbine. *Renew Energy*, 2015, 78: 386-397.
- [5] J López-Puente, R Zaera, C Navarro. The effect of low temperatures on the intermediate and high velocity impact response of CFRPs. *Compos. Part B-Eng.*, 2002, 33(8): 559-566.
- [6] D D R Cartie, P E Irving. Effect of resin and fibre properties on impact and compression after impact performance of CFRP. *Compos. Part A- Appl. S.*, 2002, 33(4): 483-493.
- [7] A Kim, I Kim. Solid particle erosion of CFRP composite with different laminate orientations. *Wear*, 2009, 267(11): 1922-1926.
- [8] X Xie, Y F Zhu, Y G Shen. Study on vibration of long-span cable-stayed bridge with steel and CFRP cables due to moving vehicles. *Eng. Mech.*, 2007, 24: 53-61.
- [9] M Wicklein, S Ryan, D M White, et al. Hypervelocity impact on CFRP: testing, material modelling, and numerical simulation. *Int. J. Impact Eng.*, 2008, 35(12): 1861-1869.
- [10] S Ryan, F Schaefer, W Riedel. Numerical simulation of hypervelocity impact on CFRP/Al HC SP spacecraft structures causing penetration and fragment ejection. *Int. J. Impact Eng.*, 2006, 33(1): 703-712.
- [11] K Iqbal, S U Khan, A Munir, et al. Impact damage resistance of CFRP with nanoclay-filled epoxy matrix. *Compos. Sci. Technol.*, 2009, 69(11): 1949-1957.
- [12] S Heimbs, S Heller, P Middendorf, et al. Low velocity impact on CFRP plates with compressive preload: Test and modelling. *Int. J. Impact Eng.*, 2009, 36(10): 1182-1193.
- [13] P Gao, X Gu, A S Mosallam. Flexural behavior of preloaded reinforced concrete beams strengthened by prestressed CFRP laminates. *Compos. Struct.*, 2016, 157: 33-50.
- [14] N Korneeva, V Kudinov, I Krylov, et al. Properties of fiber reinforced plastics under static and dynamic loading conditions. *Polym. Eng. Sci.*, 2017, 57(7): 693-696.
- [15] S Genna, C Leone, N Ucciardello, et al. Increasing adhesive bonding of carbon fiber reinforced thermoplastic matrix by laser surface treatment. *Polym. Eng. Sci.*, 2017, 57(7): 658-692.
- [16] D Feng, F Aymerich. Finite element modelling of damage induced by low-velocity impact on composite laminates. *Compos. Struct.*, 2014, 108: 161-171.
- [17] Y T Obaidat, S Heyden, O Dahlblom. The effect of CFRP and CFRP/concrete interface models when modelling retrofitted RC beams with FEM. *Compos. Struct.*, 2010, 92(6): 1391-1398.
- [18] Y He, G Tian, M Pan, et al. Impact evaluation in carbon fiber reinforced plastic (CFRP) laminates using eddy current pulsed thermography. *Compos. Struct.*, 2014, 109: 1-7.
- [19] Y He, R Yang, H Zhang, et al. Volume or inside heating thermography using electromagnetic excitation for advanced composite materials. *Int. J. Therm. Sci.*, 2017: 41-49.
- [20] Y He, R Yang. Eddy current volume heating thermography and phase analysis for imaging characterization of interface delamination in CFRP. *IEEE T. Ind. Inform.*, 2015, 11(6): 1287-1297.
- [21] Y Petronyuk, E Morokov, V Levin, et al. Study of failure mechanisms of CFRP under mechanical load by impulse acoustic microscopy. *Polym. Eng. Sci.*, 2017, 57(7): 703-708.
- [22] S Boccardi, G M Carlomagno, N D Boffa, et al. Infrared thermography to locate impact damage in thin and thicker carbon/epoxy panels. *Polym. Eng. Sci.*, 2017, 57(7): 657-664.
- [23] B W Jang, S O Park, Y G Lee, et al. Detection of impact damage in composite structures using high speed FBG interrogator. *Adv. Compos. Mater.*, 2012, 21(1): 29-44.

- [24] B W Jang, Y G Lee, C G Kim, et al. Impact source localization for composite structures under external dynamic loading condition. *Adv. Compos. Mater.*, 2015, 24(4): 359-374.
- [25] B W Jang, C G Kim. Impact localization on a composite stiffened panel using reference signals with efficient training process. *Compos. Part B-Eng.*, 2016, 94: 271-285.
- [26] B W Jang, C G Kim. Real-time detection of low-velocity impact-induced delamination onset in composite laminates for efficient management of structural health. *Compos. Part B-Eng.*, 2017, 123(15): 124-135.
- [27] R Palazzetti, A Zucchelli, I Trendafilova. The self-reinforcing effect of Nylon 6, 6 nano-fibres on CFRP laminates subjected to low velocity impact. *Compos. Struct.*, 2013, 106: 661-671.
- [28] R Palazzetti, A Zucchelli, C Gualandi, et al. Influence of electrospun Nylon 6, 6 nanofibrous mats on the interlaminar properties of Gr-epoxy composite laminate. *Compos. Struct.*, 2012, 94(2): 571-579.
- [29] R Palazzetti, X Yan, A Zucchelli. Influence of geometrical features of electrospun nylon 6, 6 interleave on the CFRP laminates mechanical properties. *Polym. Composite*, 2014, 35(1): 137-150.
- [30] H Saghafi, A Zucchelli, R Palazzetti, et al. The effect of interleaved composite nanofibrous mats on delamination behavior of polymeric composite materials. *Compos. Struct.*, 2014, 109: 41-47.
- [31] H Saito, M Morita, K Kawabe, et al. Effect of ply-thickness on impact damage morphology in CFRP laminates. *J. Reinf. Plast. Comp.*, 2011, 30(13): 1097-1106.
- [32] Y Aoki, K Yamada, T Ishikawa. Effect of hygrothermal condition on compression after impact strength of CFRP laminates. *Compos. Sci. Technol.*, 2008, 68(6): 1376-1383.
- [33] K Morioka, Y Tomita. Effect of lay-up sequences on mechanical properties and fracture behavior of CFRP laminate composites. *Mater. Charact.*, 2000, 45(2): 125-136.
- [34] M Masoumi, I F de Barros, L F G Herculano, et al. Effect of microstructure and crystallographic texture on the Charpy impact test for maraging 300 steel. *Mater. Charact.*, 2016, 120: 203-209.
- [35] Y T Tsai, H T Chang, B M Huang, et al. Microstructural characterization of Charpy-impact-tested nanostructured bainite. *Mater. Charact.*, 2015, 107: 63-69.
- [36] Z Cai, Z Chen, H Qian, et al. Impact fretting wear behavior of 304 stainless steel thin-walled tubes under low-velocity. *Tribol. Int.*, 2017, 105: 219-228.
- [37] Y Lin, Z Cai, Z Chen, et al. Influence of diameter-thickness ratio on alloy Zr-4 tube under low-energy impact fretting wear. *Materials Today Communications*, 2016, 8: 79-90.
- [38] Y Sun, Z Cai, Z Chen, et al. Impact fretting wear of Inconel 690 tube with different supporting structure under cycling low kinetic energy. *Wear*, 2017, 376: 625-633.

Submit your manuscript to a SpringerOpen[®] journal and benefit from:

- Convenient online submission
- Rigorous peer review
- Open access: articles freely available online
- High visibility within the field
- Retaining the copyright to your article

Submit your next manuscript at ► [springeropen.com](https://www.springeropen.com)